

# Three-dimensional collapse and steady flow in thick-walled flexible tubes

A. Marzo<sup>a</sup>, X.Y. Luo<sup>b,\*</sup>, C.D. Bertram<sup>c</sup>

<sup>a</sup>*Department of Mechanical Engineering, University of Sheffield, Sheffield, UK*

<sup>b</sup>*Department of Mathematics, University of Glasgow, Glasgow, UK*

<sup>c</sup>*Graduate School of Biomedical Engineering, University of New South Wales, Sydney, Australia*

Received 8 March 2004; accepted 10 March 2005

---

## Abstract

Three-dimensional collapse of and steady flow through finite-length elastic tubes are studied numerically. The Navier-Stokes equations coupled with large, nonlinear deformation of the elastic wall are solved by using the finite-element software, FIDAP. Three-dimensional solid elements are used for the elastic wall, allowing us to specify any wall thickness required. Plane-strain results for the cross-sectional shape of thinner-walled tubes are validated by comparison with published numerical data. Three-dimensional results for flow through finite-thickness tubes are in excellent agreement with published numerical results based on thin-shell elements, and are used to show the effects of varying wall thickness. Finally, the computational predictions are compared with experimental pressure–area relationships for thick-walled tubes. The simulations confirm a previously neglected experimental finding, that the Young wavespeed can be lower between buckling and osculation for thick tubes than for thinner ones.

© 2005 Elsevier Ltd. All rights reserved.

*Keywords:* Collapsible tube flow; Finite element methods; Buckling; Wavespeed

---

## 1. Introduction

Many physiological conduits transport viscous fluids within our body. Because of their high flexibility, these conduits may collapse nonaxisymmetrically under particular conditions of external and internal fluid pressure. When this phenomenon occurs, the buckled vessels become very flexible and small changes in transmural pressure  $P_{tm}$  (internal minus external pressure) may induce large displacements. This strong interaction between fluid and structure gives rise to a number of interesting phenomena, including flow-rate limitation, pressure-drop limitation and a tendency to self-excited oscillation.

In the cardiovascular system, veins above the level of the heart and outside the skull collapse due to hydrostatic reduction of blood pressure. This assumes particular importance in subjects with long necks, especially giraffes (Brook and Pedley, 2002). Flow-induced collapse of cardiovascular vessels is believed to play an important role in the supply of blood to many internal organs (Guyton and Adkins, 1954; Rodbard, 1966). Moreover, dynamic flow-induced collapse of blood vessels downstream of atherosclerotic stenoses may cause plaque rupture, which can lead to the occlusion of

---

\*Corresponding author. Tel.: +44 141 330 4746; fax: +44 141 330 4111.

E-mail address: x.y.luo@maths.gla.ac.uk (X.Y. Luo).

the vessel lumen distally, with potentially lethal consequences in the case of the carotid artery (Binns and Ku, 1989; Ku, 1997). In the large airways, flow-induced oscillations are believed to give rise to a number of different noises with important diagnostic value. Controlled self-excited oscillations also play a fundamental role in speech production (Berke et al., 1991). During micturition, the urethra behaves like a collapsible tube, and accordingly can exhibit flow-limitation effects (Griffiths, 1971).

Given its importance and complexity, the topic of flow through collapsible tubes has been studied for over 30 years. However, the full understanding of this physical phenomenon still represents an unsolved challenge. Kamm and Pedley (1989) reviewed the subject briefly; a more comprehensive review of the biological examples and the theoretical and computational developments is given by Heil and Jensen (2003), while Bertram (2003) has reviewed the experimental side of the subject, and applications in medicine and technology. Experimental investigations on a Starling resistor prototype of the system have revealed a rich dynamic behaviour, with various types of self-excited oscillations (Bertram et al., 1991; Bertram and Elliott, 2003). To reveal the mechanisms of such oscillations, much work has been carried out, but most is limited to 1-D or 2-D models (Pedley, 1992; Luo and Pedley, 1995, 1996, 1998, 2000; Cai and Luo, 2003; Jensen and Heil, 2003).

One-dimensional models adopt a large number of ad hoc assumptions that limit any systematic improvement. Two-dimensional models of a collapsible channel are based on a more rational approach, and in principle could be realized in a laboratory. However, only a 3-D study can provide the full picture of a collapsible tube, which exhibits strongly 3-D behaviour. Owing to the extensive computational resources required and the high nonlinearity of the system, to date there is only limited published work on 3-D thin-walled tubes. Hazel and Heil (2003) investigated the steady flow through thin-walled elastic tubes for a finite Reynolds number. In their finite-element approach, they solved the steady 3-D Navier–Stokes equations simultaneously with the equations of geometrical nonlinear, Kirchhoff–Love thin-shell theory. One of the assumptions underlying thin-shell theory is that the wall thickness of the tube is some 20 or more times smaller than its radius. Considering that much experimental work is on thick-walled tubes (Bertram, 1987; Bertram and Castles, 1999), it is important that 3-D numerical simulations are not restricted to thin-shell theory.

In this paper, we present 3-D numerical simulations for a finite-Reynolds-number steady flow in thick-walled tubes, using the finite-element software FIDAP (2002) (Fluent Inc.).

## 2. Methods

We model the steady flow at Reynolds number  $Re$  of a viscous fluid through a thick-walled deformable tube of undeformed radius  $R$ , wall thickness  $h$ , and length  $L$ . The tube wall material has Poisson's ratio  $\nu$  and Young's modulus  $E$ . The fluid is assumed to be incompressible, with density  $\rho$ , and Newtonian, with viscosity  $\mu$ . The computational geometry is shown in Fig. 1.

The problem was formulated in Cartesian coordinates  $(x, y, z)$ , with  $z$  chosen to be the direction of the tube axis, while  $x$  and  $y$  are the transverse coordinates. The origin is fixed at the centre of the collapsible-tube inlet. In order to apply the boundary conditions at inlet and outlet of the computational domain properly, and to mimic the experimental set-up, rigid tubes were added upstream and downstream of the deformable extension. The lengths of the upstream and downstream rigid extension are  $L_{up}$  and  $L_{down}$ , respectively. The pressure acting on the external walls of the deformable tube is  $p_{ext}$ .

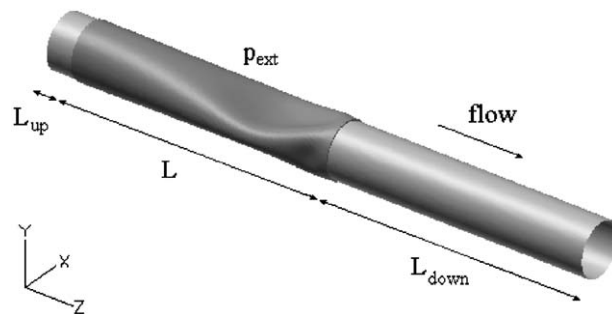


Fig. 1. The geometry of the collapsible tube.

2.1. Fluid–solid coupling

The fluid/structure-interaction (FSI) algorithm treats the equations that solve the structural problem, the remeshing problem and the fluid problem by a staggered approach; that is to say, the algorithm solves the equations in sequence. The overall computational procedure adopted to solve FSI problems that involve large displacement is depicted in Fig. 2.

Firstly, the equations governing the fluid are solved for fluid velocity and pressure fields. Subsequently the traction, i.e. pressure and viscous stress, is calculated at the interface between fluid and structure. The traction is then applied to the structure together with the other boundary conditions, and the structural equations are solved for the displacement of the structure. At this point the position of the wetted surface is updated. Finally, the equations that describe the mesh displacement are solved by imposing the displacement of the wetted surface as boundary condition. This cycle is repeated until convergence is achieved.

2.2. Equations governing the fluid

The Navier–Stokes equations are used for the fluid

$$\rho u_i u_j = \sigma_{ij,j}, \tag{1}$$

$$u_{j,j} = 0, \tag{2}$$

where  $i, j = 1, 2, 3$ ,  $u_i$  is velocity,  $\rho$  is density, and  $\sigma_{ij}$  is the stress tensor. The stress tensor can be written as

$$\sigma_{ij} = -p\delta_{ij} + \tau_{ij}, \tag{3}$$

where  $p$  is the pressure,  $\tau_{ij}$  is the deviatoric stress tensor, and  $\delta_{ij}$  is the Kronecker delta. For viscous, incompressible fluids the constitutive relation has the form

$$\tau_{ij} = 2\mu s_{ij}, \tag{4}$$

where  $\mu$  is the viscosity of the fluid and  $s_{ij}$  is the strain rate tensor defined as

$$s_{ij} = \frac{1}{2}(u_{i,j} + u_{j,i}). \tag{5}$$

No-slip boundary conditions are fixed on the tube walls

$$u_1 = u_2 = u_3 = 0.$$

A fully developed Poiseuille parabolic velocity profile is used for the inlet,

$$u_1 = u_2 = 0, \quad u_3 = 2U \left[ 1 - \frac{1}{R^2} (x^2 + y^2) \right] \quad \text{at } z = -L_{up},$$

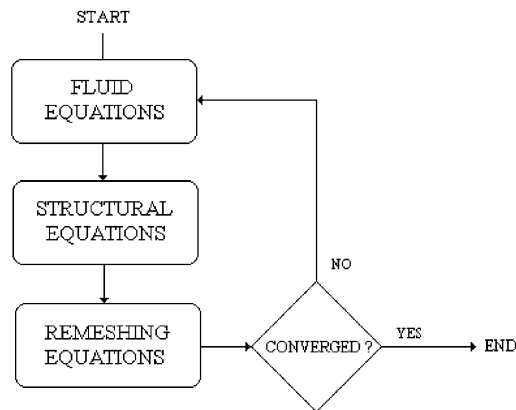


Fig. 2. Strategy of the computational procedure in FIDAP.

where  $U$  represents the velocity averaged across the undeformed cross-sectional area. A parallel, axially traction-free outflow is fixed at the outlet

$$u_1 = u_2 = 0, \quad -p + 2 \frac{\partial u_3}{\partial z} = 0 \quad \text{at } z = L + L_{\text{down}}.$$

### 2.3. Equations governing the structure

We assume that the strain of the wall is small, and this allows us to treat the structure as an elastic and linear medium. The overall structural behaviour is described by the momentum Eq. (6), the equilibrium Eq. (7) and the constitutive Eqs. (8) and (9)

$$\sigma_{ij,j} = 0, \quad (6)$$

$$\sigma_{ij} n_j = {}^s \bar{t}_i, \quad (7)$$

$$\sigma_{ij} = D_{ijkl} \varepsilon_{kl}, \quad (8)$$

$$\varepsilon_{kl} = \frac{1}{2} (d_{k,l} + d_{l,k}), \quad (9)$$

where  $\sigma_{ij}$  is the Cauchy stress tensor,  ${}^s \bar{t}_i$  is the externally applied surface traction vector,  $n_j$  is the outward pointing normal vector,  $D_{ijkl}$  is the material (Lagrangian) elasticity tensor, and  $\varepsilon_{kl}$  is the infinitesimal strain tensor. The wall deformation is thus governed by the principle of virtual displacements

$$\int_{{}^s \Omega} \sigma_{ji} \delta d_{i,j} \, d\Omega = \int_{{}^s \Omega} \rho_w \bar{f}_i \delta d_i \, d\Omega + \int_{{}^s \Gamma} {}^s \bar{t}_i \delta d_i \, d\Gamma, \quad (10)$$

where  $\rho_w$  represents the material density,  $\delta d_i$  is the virtual displacement vector,  $\bar{f}_i$  is an externally applied body force vector,  ${}^s \bar{t}_i$  is the externally applied surface traction vector,  ${}^s \Omega$  is the domain occupied by the moving elastic structure, and  ${}^s \Gamma$  is the boundary of the structure. This formulation is nonlinear because, at any iteration, the current domain,  ${}^s \Omega$ , is unknown. Thus, at each iteration, the solution is calculated using an incremental Lagrangian formulation. At each stage, the stresses and strain are measured with respect to the most recent available configuration (updated Lagrangian approach).

We assume that the deformable part of the tube is clamped at both ends

$$dx = dy = dz = 0 \quad \text{at } z = 0, L.$$

### 2.4. Remeshing equations

The remeshing problem is solved by considering the mesh as a pseudo-elastic medium, the deformation of which is based on the boundary conditions resulting from the displacement solution of the structural problem. In fact, the elasticity-based remeshing algorithm is similar to that employed to solve the structural problem. However, in the remeshing algorithm, only displacement boundary conditions are allowed (boundary conditions involving stresses or forces proportional to the displacement have no meaning in the mesh context).

### 2.5. Numerical implementation

We discretize the structural domain with 3-D solid elements. All six possible stresses (three normal and three shear components) are taken into account. Shell theory in general (there are several formulations of thin-shell theory) does not take account of normal stress in the wall thickness direction. This is reasonable if the thickness is small in comparison with other dimensions. In many of Bertram's experiments, in order to avoid the well-known problem of the collapsible part being sucked into the downstream rigid tube, the wall thickness is relatively large. Using a 3-D solid element enables us to compare our numerical results with Bertram's experimental data. However, this is done at the cost of demanding much greater computational resources, and of a propensity to ill-conditioning and locking behaviour when used for 'thinner-walled' tubes.

Due to the extensive computation required and also since in experiments elastic tubes of substantial length usually collapse into a mode-2 buckling, here we only consider one quarter of the whole domain. The computational domain is

symmetric about the planes  $x = 0$  and  $y = 0$ . A finite element mesh is shown in Fig. 3. For a typical problem, the mesh was discretized with 5000 geometrically nonlinear isoparametric 3-D solid elements (27 nodes for each element), giving 30 000 nodal points with seven degrees of freedom at each node (three for displacements, three for velocity and the pressure) for each fluid element, and only three degrees of freedom (displacements) for each structural element. The velocity and displacement fields were approximated using triquadratic interpolation functions, while the pressure approximation was linear. The Galerkin form of the method of weighted residuals was used to reduce the discretization errors to zero. Inherent instability deriving from the application of the Galerkin finite-element method was stabilized using a streamline upwinding scheme and relaxation factors for the fluid variables. The fluid equations were solved using a segregated approach (i.e. the global problem is decomposed into a system of sub-matrices that is solved sequentially for each unknown) using the pressure-projection method. Finally, the linear systems derived from the application of the Galerkin finite element method were solved using direct Gaussian elimination.

In order to validate our results against published thin-shell results, we need to be able to model ‘thinner-walled’ tubes as well. Modelling thinner-walled tubes with 3-D solid elements presented some difficulties. With a thinner-walled tube, it is extremely difficult to maintain the aspect ratio of each element within reasonable values without generating a finer-than-necessary discretization of the fluid mesh. Therefore, we had to reach a compromise between a reasonably economical mesh and a moderate aspect ratio.

All the simulations were run on a Sun V880, with eight 900 MHz UltraSPARC III+ processors and 32 GB of main memory. A typical analysis performed with a mesh involving approximately 210 000 dof required on average 14 s of CPU time per iteration. Convergence, defined here as a relative change in the solution from one iteration to the next of less than  $10^{-6}$ , was usually achieved within 450 iterations. The effective (real) time required to achieve convergence can be reduced by distributing the computation between two or more processors through the parallelization of the algorithm.

As the axisymmetric solution was extremely robust, it was necessary to add a perturbation load in order to make the structure collapse into a mode-2 buckling. The perturbation load was applied together with the external pressure load, as shown in Fig. 4. The total (perturbation plus uniform) load was defined as

$$p_{\text{load}} = a_0 + a_1 x^2, \quad (11)$$

where  $x$  is the spatial coordinate as shown in Fig. 4, and the coefficients  $a_0$  and  $a_1$  were chosen to be

$$a_0 = p_{\text{ext}} + C, \quad a_1 = -\frac{C}{(R+h)^2}. \quad (12)$$

The value of the parameter  $C$ , which regulates the desired degree of perturbation, was gradually set to zero once the structure had buckled.

When the structure was severely collapsed, to avoid negative volumes occurring during the remeshing, it was necessary to start from an optimal mesh configuration in order to avoid elements with large aspect ratio, especially where large displacements were expected. An automatic procedure provided in FIDAP for stiffening the mesh elements was used to control mesh distortion. The procedure is based upon a check of the level of distortion of the elements. When an element is found to be distorted (here, mostly in the flow region near the wetted surface, where the structure undergoes large displacements), it is made stiffer relative to the others by the assignment of a higher value of elasticity

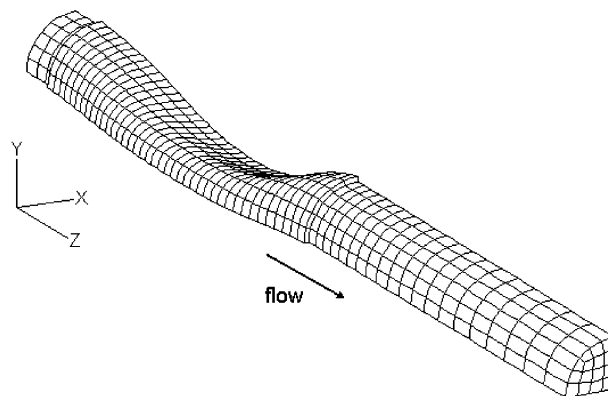


Fig. 3. The finite element mesh for a tube with  $h/R = \frac{2}{20}$  and  $Re = 350$ .

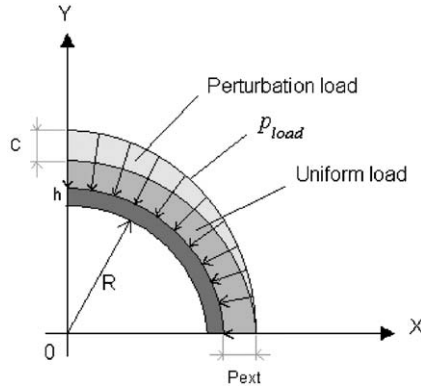


Fig. 4. The perturbation load applied on the external surface of the tube.

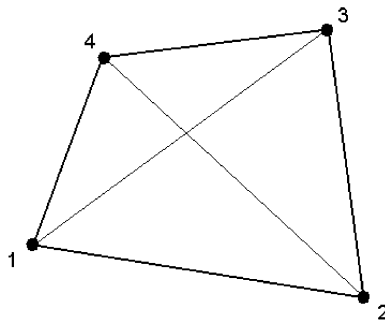


Fig. 5. 4-noded quadrilateral element.

modulus for the mesh, thus preventing further deformation that can lead to the breakdown of the mesh. (What is changed here is a fictitious Young’s modulus used to treat the fluid mesh as a pseudo-elastic material. The procedure controls only the deformation of fluid elements, and does not affect the actual structural displacement and flow fields.) The method for computing the distortion depends on the element type. For simplicity, we here consider the case of a 4-noded quadrilateral element. The same procedure is easily extended to other element types.

The 4-noded quadrilateral element, as shown in Fig. 5, is divided into four overlapping triangles:  $\Delta_1 = \Delta_{\{1,2,4\}}$ ,  $\Delta_2 = \Delta_{\{1,2,3\}}$ ,  $\Delta_3 = \Delta_{\{2,3,4\}}$ , and  $\Delta_4 = \Delta_{\{1,3,4\}}$ . The code employs a scalar distortion parameter to indicate element quality. First, the aspect ratio of each triangle is measured. The aspect ratio is defined as

$$\Phi_{\Delta} = \frac{R_{\Delta}}{r_{\Delta}},$$

where  $R_{\Delta}$  is the radius of the triangle’s circumcircle and  $r_{\Delta}$  that of its incircle. The distortion parameter,  $\Phi_{el}$ , is then defined by the norm

$$\Phi_{el} = \max(\Phi_{\Delta_l}).$$

where  $l = 1, 2, 3, 4$ . A control parameter then measures the change in  $\Phi_{el}$  through the iterative process by

$$\bar{\Phi}_{el} = \frac{\Phi_{el}^k}{\Phi_{el}^0},$$

where  $k$  is the iteration count and 0 represents the initial mesh. The pseudo-elastic Young’s modulus of each fluid mesh element is finally calculated by

$$E_{el} = E^0(\bar{\Phi}_{el})^n,$$

where  $E^0$  and  $n$  are inputs of the problem (typical values used in this work were 1 Pa and 2.5 for initial Young's modulus and power coefficient, respectively), and  $\bar{\Phi}_{el}$  is calculated by the code. Further details can be found in Bar-Yoseph et al. (2001).

Mesh-independence testing was done by repeating selected analyses using finer discretizations; see Appendix A.

### 3. Results

#### 3.1. Plane-strain buckling analysis of a tube cross-section

The structural capabilities of the code were first tested by performing the computational analysis of a cylindrical unsupported tube subjected to a uniform external pressure. We considered a thinner-walled tube of Young's modulus  $E = 10^5$  Pa, Poisson's ratio  $\nu = 0.4$ , undeformed internal radius  $R = 5$  mm, wall thickness  $h = 0.1$  mm and infinite length. The total load applied incrementally to the structure was  $p_{\text{ext}} = 0.5$  Pa.

The numerical problem was simplified by reducing it to a plane-strain analysis. The computational domain was discretized with 900 geometrically nonlinear quadrilateral 9-noded elements, giving 3819 nodes with 2 dof at each node (the two components of displacement). The mesh and the imposed boundary conditions are shown in Fig. 6.

The total pressure load was applied incrementally in 10 000 steps. To avoid solving a contact problem, the simulation was stopped a few steps before the osculation of the opposite walls of the tube. The computational results are compared to the numerical results by Flaherty et al. (1972), as shown in Fig. 7. For convenience, we use below the nondimensional transmural pressure defined as  $\bar{p} = p_{\text{ext}}/P_k$ , where  $P_k = Eh^3/[12(1-\nu^2)R^3]$ . First opposite-wall contact occurred in our simulation at  $\bar{p} = 5.033$ , which is slightly lower than the value obtained by Flaherty et al. (1972). There is in general very good agreement with the cross-sectional area after tube buckling.

#### 3.2. 3-D analysis of fluid flow through a thinner-walled collapsible tube

In their recent study, Hazel and Heil (2003) used thin-shell theory and the finite-element method to simulate finite-Reynolds-number flows in collapsible tubes. For validation purposes it is useful to compare our computation for thinner-walled tubes with their results. To study the effect of fluid inertia on the tube deformation, Hazel and Heil (2003) obtained numerical predictions for two different flow conditions:  $\text{Re} = 0$  and 128.

Here, we follow Hazel and Heil and use  $R = 4$  mm,  $L_{\text{up}} = R$ ,  $L = L_{\text{down}} = 10R$ ,  $\nu = 0.49$ , and  $h/R = \frac{1}{20}$ . In order to make a meaningful comparison between the two flow conditions,  $\text{Re} = 0$  and 128, we set  $E = 0.0045594$  Pa,  $p_{\text{ext}} = 1.19 \times 10^{-6}$  Pa for  $\text{Re} = 0$ , and  $E = 4559.4$  Pa,  $p_{\text{ext}} = 1.4$  Pa for  $\text{Re} = 128$ , to achieve the same nondimensional parameters used by Hazel and Heil (2003). These choices lead to the same degree of collapse (maximum displacement in  $y$ -direction) for the two  $\text{Re}$  values.

The comparison between our results and those of Hazel and Heil (2003) is shown in Fig. 8. The axial coordinates are scaled to the radius and the pressure is scaled to the bending stiffness. Excellent agreement is achieved for both flow conditions.

The displacements for the two flow conditions are shown in Fig. 9.

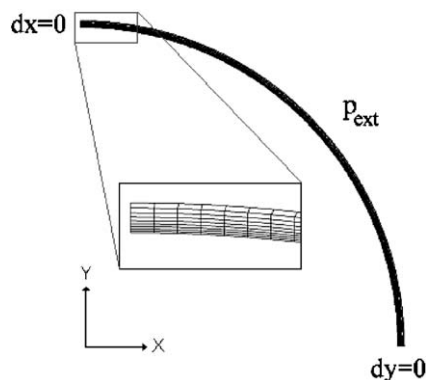


Fig. 6. The finite-element mesh for the tube cross-section and the boundary conditions specified for the plane-strain analysis.

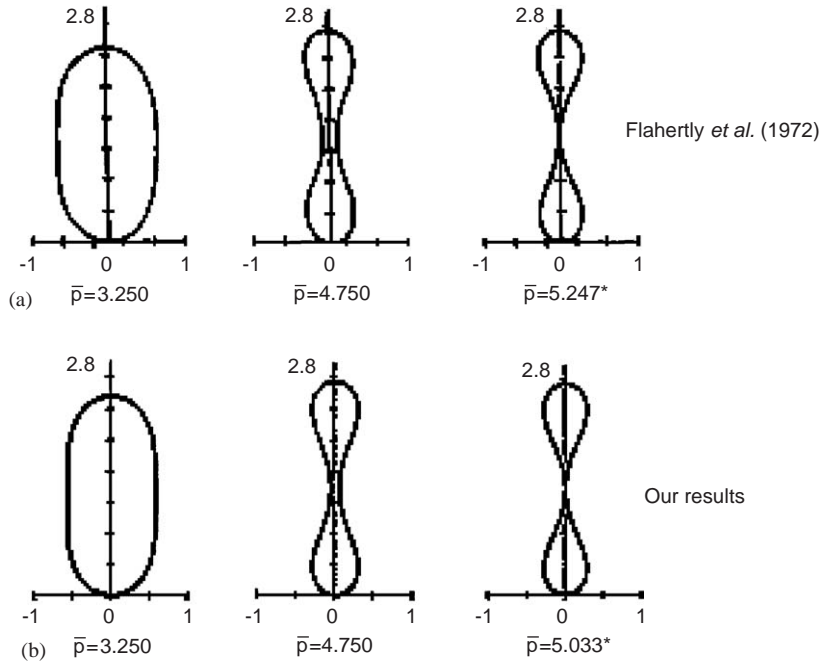


Fig. 7. Comparison between our and previously published predictions by Flaherty et al. (1972) of the post-buckling patterns;  $\bar{p}$  is the nondimensional transmural pressure. (a) Post-buckling patterns from Flaherty et al. (1972); (b) post-buckling patterns from our plane-strain analysis. The asterisks indicate the values when the first opposite-wall contact occurred.

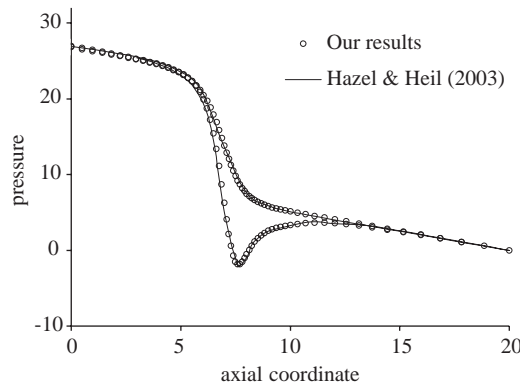


Fig. 8. Pressure drop along the tube axis for two flow conditions,  $Re = 0$  (upper) and  $Re = 128$  (lower). The variables are nondimensionalized in the same way as did Hazel and Heil (2003).

3.3. Wall-thickness influence on structural displacement and flow behaviour

We also performed simulations for tubes of differing thickness:  $h/R = \frac{1}{20}$  (close to the upper limit of thin-shell theory validity) and  $h/R = \frac{2}{20}$ . In all cases presented in this section, unless otherwise stated, we use  $R = 4\text{ mm}$ ,  $L_{up} = R$ ,  $L = L_{down} = 10R$ ,  $\nu = 0.49$ ,  $E = 4559.4\text{ Pa}$  and  $Re = 128$ .

In the first test, two different values of external pressure were gradually applied until a similar degree of collapse, where the maximum radial deformation is equal to 80% of the undeformed radius, was achieved in both cases. This was achieved by setting  $p_{ext} = 1.4\text{ Pa}$  for  $h/R = \frac{1}{20}$  and  $p_{ext} = 3.3\text{ Pa}$  for  $h/R = \frac{2}{20}$ . The results are shown in Fig. 10.

Although the maximum degree of collapse is the same, the point of maximal collapse is closer to the centre of the tube (around  $z/L = 0.63$ ; see Figs. 10(b) and 11) owing to the higher extensional stiffness of the thick-walled tube. In the

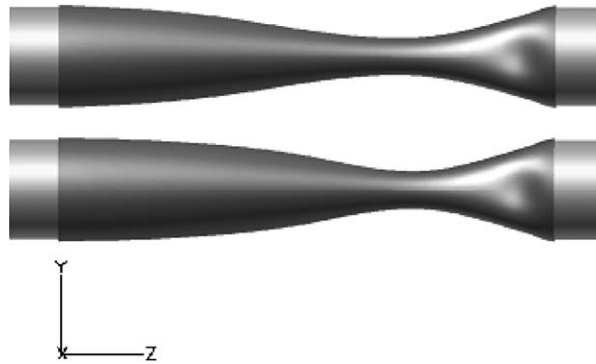


Fig. 9. The displacement solution for  $Re = 0$  (upper) and  $Re = 128$  (lower).

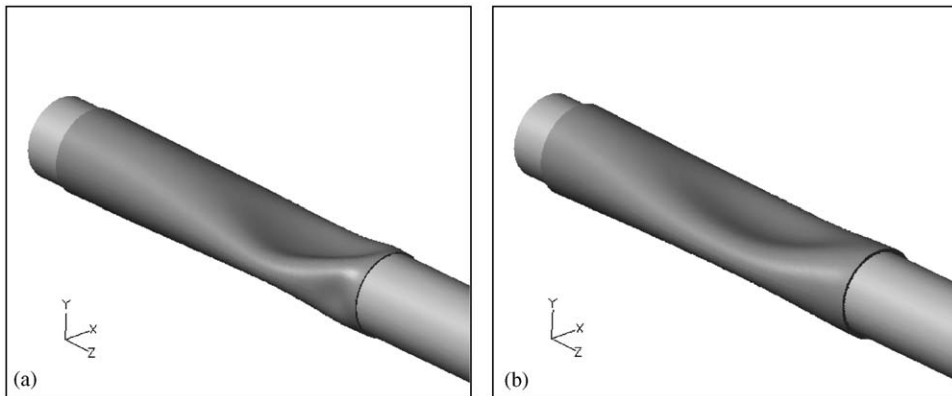


Fig. 10. Tube configurations for (a)  $p_{ext} = 1.4 \text{ Pa}$  with  $h/R = \frac{1}{20}$  and (b)  $p_{ext} = 3.3 \text{ Pa}$  with  $h/R = \frac{2}{20}$ . The degree of collapse for both cases is 80%.

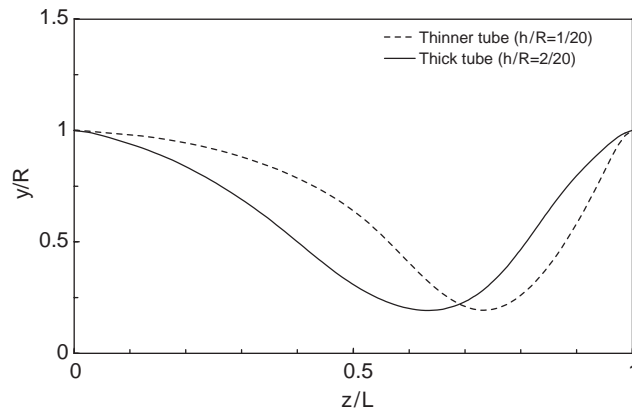


Fig. 11. Displacements of the edge given by the intersection of the symmetry plane  $x = 0$  with the wetted surface for the thick-walled and thinner-walled tubes.

thinner-walled case (Figs. 10(a) and 11), the point of greatest collapse occurs further downstream (around  $z/L = 0.74$ ), and a small secondary buckling pattern develops at the downstream end. The thick-walled tube does not exhibit this behaviour under these conditions.

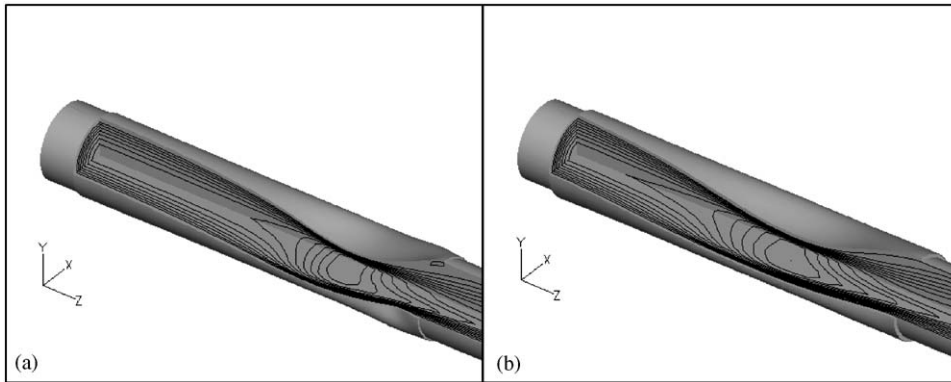


Fig. 12. Axial-velocity contours are plotted for (a) the thinner-walled, and (b) the thick-walled tube at  $Re = 128$ . Flow separation is observed in the thinner-walled tube flow.

The high degree of collapse strongly influences the fluid flow pattern. Fig. 12 depicts axial velocity contours along the symmetry planes of the computational domain and in the transverse cross-section at the collapsible-tube inlet for the two cases under study. Both the location of the greatest collapse and the deformed wall shape have a direct effect on the flow patterns. In the case of the thicker wall, the increase in axial velocity starts further upstream. However, because the displacement gradient along the  $z$ -axis in the thick-walled tube is smaller compared with the thinner-walled tube, the flow change is less severe: there is no flow separation downstream, unlike the thinner-walled tube, and the maximum axial velocity is slightly smaller. In both cases, in the most collapsed section of the tube, the smaller cross-sectional area is associated with higher-speed fluid flow, which splits into two jets. These jets are formed by the concurrent effect of increased viscous retardation due to the boundary layers of the inwardly buckled walls.

We next applied the same external pressure,  $p_{\text{ext}} = 1.4 \text{ Pa}$ , to both the differing-thickness tubes. The tube parameters were otherwise unchanged. In the case of the thick-walled tube, the external pressure was then insufficient to make the tube collapse, and the flow pattern therefore retained its Poiseuille profile.

Bertram and Godbole (1997) measured the fluid flow at  $Re = 705$  in a rigid deformed tube resembling the collapsed state of an elastic tube conveying a flow. They used laser Doppler anemometry to measure the axial velocity component and one transverse velocity component at several axial locations upstream and downstream of the constriction. For a relatively high degree of collapse (close to the point of opposite-wall contact), it was observed that the flow splits into two jets that impinge on the vertical sidewalls of the tube (parallel to the  $x = 0$  symmetry plane in the coordinates used here) and spread vertically into a crescent shape. With further diffusion of momentum, the flow downstream then became annular in cross-section, with forward flow near the wall surrounding a central region of low flow, before the velocity profile reverted to parabolic. For a flow with lower  $Re$ , somewhat equivalent phenomena were numerically predicted by Hazel and Heil (2003).

In order to study the influence of the wall thickness on the development of the two jets, two new cases are here considered. The geometries used here are the same as those used previously for the thinner-walled and thick-walled tubes. We set  $Re = 350$ ,  $E = 3 \text{ MPa}$ ,  $\nu = 0.3$  to improve convergence and to remain close to the nondimensional parameters used by Hazel and Heil (2003). A degree of collapse of 86.4% was imposed on the two tubes by applying  $p_{\text{ext}} = 520 \text{ Pa}$  for  $h/R = \frac{1}{20}$  and  $p_{\text{ext}} = 1550 \text{ Pa}$  for  $h/R = \frac{2}{20}$ . Fig. 13 shows the results of these computations. The point of maximum collapse is  $z/L = 0.595$  and  $0.655$  for the thick-walled and thinner-walled tube, respectively. The development of the flow in the streamwise direction is similar in the two cases, and largely agrees with what was observed by Bertram and Godbole (1997) and predicted by Hazel and Heil (2003). At the point of greatest collapse, the fluid flow spreads out along the  $x$ -axis while the peak of maximum axial velocity moves from the tube axis and develops into a line extending towards the sidewalls. Two parallel jets are then formed and axial flow subsequently develops into a rounded H-shape, with a large area of slow reversed flow near the opposite ends of the minor axis of the cross-section ( $y$ -axis). A strip of positive axial velocity divides the reversed flow areas along the  $x$ -axis and unites the two jets at locations between  $d_t = 4R$  and  $8R$ , where  $d_t$  measures distance along the  $z$ -axis downstream from the point of the maximum collapse (tube throat). However, the different displacements of the two geometries produce two slightly different developments of the two jets. In the thinner-walled-tube case the two jets impinge more on the vertical sidewalls, and the distance between them, as they develop in parallel along the tube axis, is more pronounced than in the thicker tube. A difference is also noticeable in the thickness of the strip of positive velocities which divides the two zones

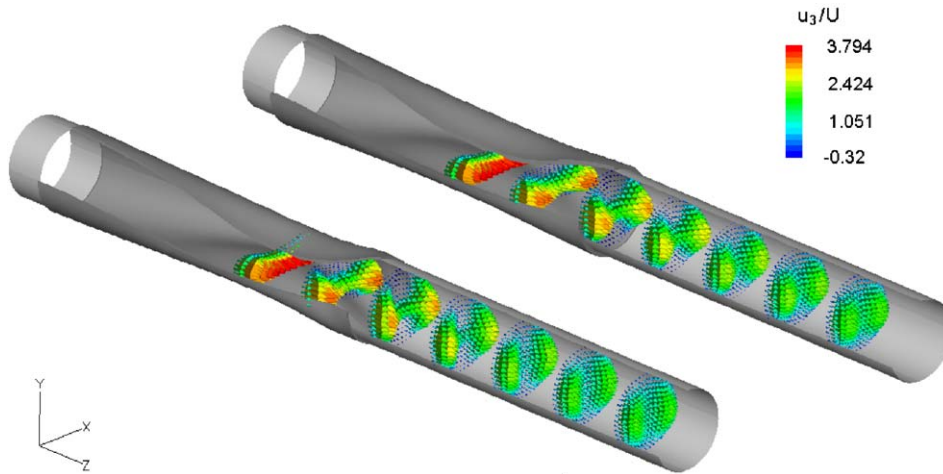


Fig. 13. 3-D vector plots of axial velocity for (left) the thinner-walled and (right) the thick-walled tube 0, 2R, 4R, 6R, 8R, 10R, and 12R downstream of the respective points of maximum collapse.  $Re = 350$ .

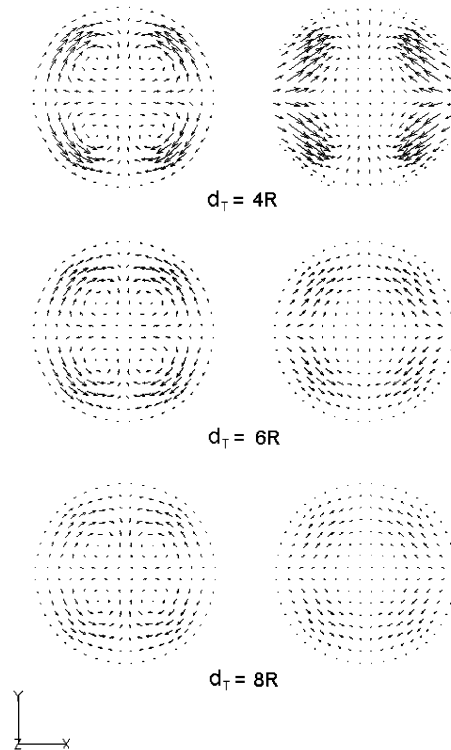


Fig. 14. Projection of velocity vectors on three cross-sections of (left) the thinner-walled and (right) the thick-walled tube. Cross-sections are located at  $d_t = 4R, 6R, 8R$  downstream of the respective points of maximum collapse. As locations relative to the tube itself, these are  $z/L = 0.995, 1.195$  and  $1.395$  for the thick-walled tube and  $z/L = 1.055, 1.255$  and  $1.455$  for the thinner-walled tube.

of reversed flow. This extends more along the minor axis of the cross-section in the thick-walled tube than in the thinner one (most noticeable at  $d_t = 4R, 6R$ ).

Fig. 14 shows details of the secondary flows that develop streamwise for the two geometries. The vectors displayed are the projection of the velocity vectors on the respective cross-sections. In the thinner-walled tube, four eddies are formed in each quadrant of the tube cross-section. Their centre of rotation moves from the tube walls towards the tube

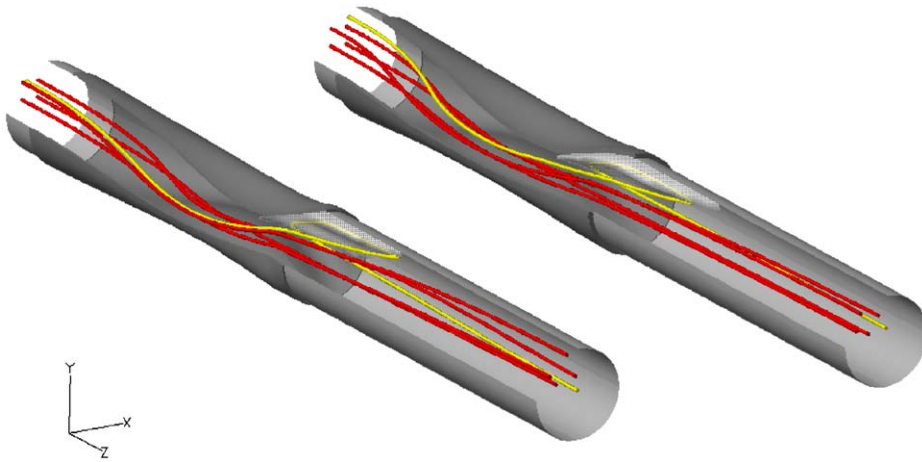


Fig. 15. Particle paths (streamlines) on one quadrant of the computational domain for (bottom left) the thinner-walled and (top right) the thick-walled tubes at  $Re = 350$ . The initial location from which each forward flow streamline develops is given in Cartesian coordinate  $(x, y, z)$  as:  $(-0.001, 0.001, 0)$ ,  $(-0.0025, 0.001, 0)$ ,  $(-0.001, 0.0025, 0)$ ,  $(-0.0025, 0.0025, 0)$ . For both cases a reversal flow streamline passing through the same point  $(0, 0.002, 0.04)$  inside the reversal zone is also shown in yellow. The actual size of the reversal zone for both flows is indicated by the light-shadowed area.

axis as  $z$  increases. Contrary to that, the displaced geometry of the thick-walled tube does not confer such a pattern to the fluid flow. The flow direction along the symmetry planes is always directed towards the centre of the cross-section.

Figs. 15 and 16 show details of the reversed flow which develops downstream of the constriction for the two geometries considered. In the thinner-walled tube case, the flow reversal zone extends from  $z/L = 0.803$  to 1.3. In the thick-walled tube case, the area occupied by reversed flow is longer, extending from  $z/L = 0.745$  to 1.338. We note from Fig. 16 that the reversed flow has four initial maxima in the thinner-walled tube, but only two in the thick-walled one. This is obviously linked to the four-eddy secondary flow for the thinner-walled tube (Fig. 14), absent in the thick-walled tube flow.

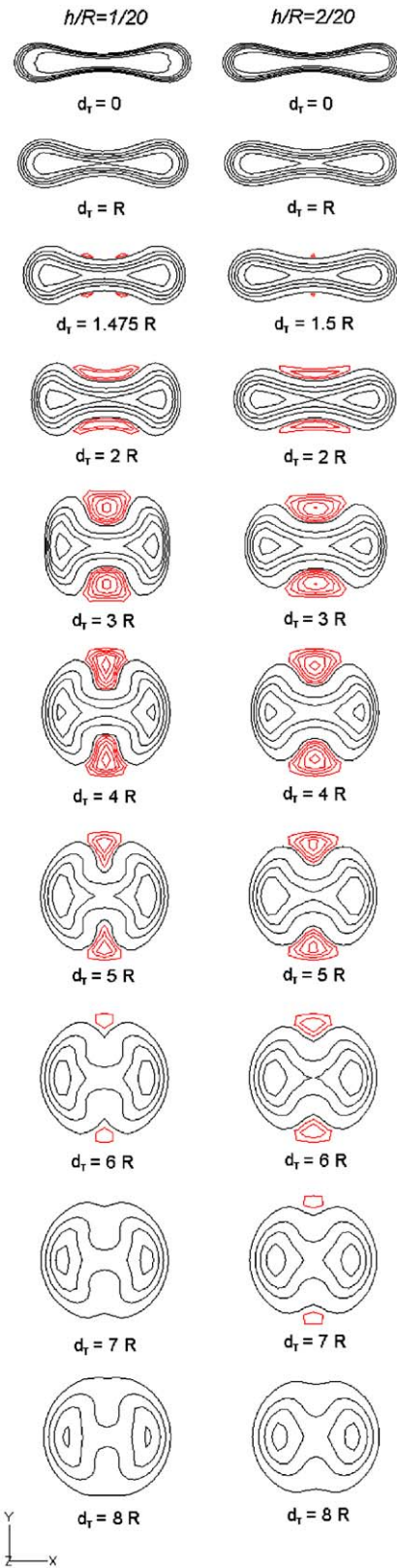
### 3.4. Comparison with experiments on thick-walled tubes

In this section, results are compared with experimental data on the pressure–area relation for two thick-walled collapsible tubes reported by Bertram (1987). Bertram measured a ‘thinner-walled’ tube, with a wall-thickness-to-inside-radius ratio ( $h/R_i$ ) of 0.38, and a ‘thick-walled’ tube with a thickness ratio of 0.50. Both of these are actually much thicker than is typically regarded as the limit of validity for a thin shell ( $h/R_i < 0.05$ ), emphasizing the importance of using a computational method able to cope with arbitrarily thick walls. In the experimental rig, a silicone-rubber tube was mounted and axially loaded between coaxial pipes forming part of a pressure chamber. Pressure within the tube was maintained constant by connecting the conduit to a source of constant head of aqueous fluid (a solution of water, sodium nitrite and anti-corrosive additives). External pressure in the chamber was varied by admitting compressed air. The internal cross-sectional area of the tube halfway along was measured by an electrical impedance method.

In the numerical investigation, the physical problem was again approximated by considering a quarter of the tube. Applying a constant pressure on the inner wall of the tube approximated the influence of the fluid on the structural behaviour. In order to stabilize the convergence behaviour of the numerical approach it was necessary to tune the load-step increment carefully.

Bertram (1987) recorded a slightly hysteretic pressure–area curve for his material; however, we assumed here that our material was perfectly elastic. Following the reported experimental conditions, the parameters of the ‘thinner-walled’

Fig. 16. Contour plots of axial velocity on seven cross-sections from the most collapsed location of the thinner-walled ( $h/R = \frac{1}{20}$ ) and the thick-walled tube ( $h/R = \frac{2}{20}$ ) at  $Re = 350$ . The reversed flow contours are plotted between  $u_3/U = -0.319$  and zero with an equal spacing of 0.0532 (red contours). The forward flow contours are plotted between  $u_3/U = 0.1$  and 3.794 with an equal spacing of 0.616 (black contours). Reversed flow first appears at  $d_t = 1.475R$  for the thinner-walled tube, and  $1.5R$  for the thick-walled one.



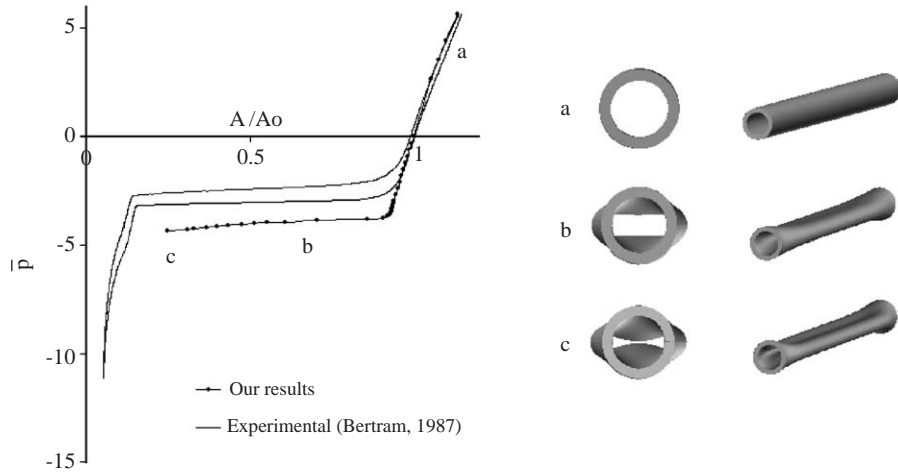


Fig. 17. The computed dimensionless pressure–area relation compared with experimental data of Bertram (1987) for the ‘thinner-walled’ tube case. The experimental data follow a hysteresis loop, with more external pressure needed to bring about collapse and less to cause recovery.

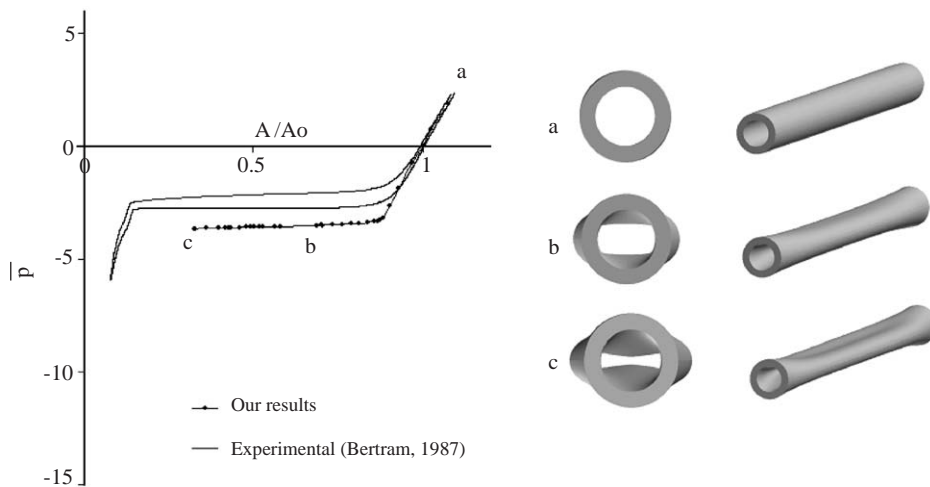


Fig. 18. The computed dimensionless pressure–area relation compared with experimental data of Bertram (1987) for the thick-walled tube case.

tube were chosen to be  $R_i = 6.35$  mm,  $h = 2.4$  mm,  $L = 230$  mm,  $E = 3.8$  MPa,  $\nu = 0.423$ , and of the ‘thick-walled’ tube,  $R_i = 6.35$  mm,  $h = 3.2$  mm,  $L = 230$  mm,  $E = 4.0$  MPa and  $\nu = 0.423$ . An axial strain of 0.7% was applied in the axial direction by imposing a pre-stretch condition of 1.61 mm beyond the undeformed length of the thinner-walled tube. The axial strain of the thick-walled tube was 0.5% and was applied by imposing a pre-stretch condition of 1.15 mm beyond its undeformed length. Each computational result, represented by a point in the pressure–area relation, was computed starting from a previous converged analysis. The transmural pressure difference was varied in the range  $\bar{p} = -4.34$  to 5.64 for the thinner-walled tube, and  $\bar{p} = -3.65$  to 2.23 for the thick-walled tube, respectively. This range excluded pressure values which would bring the tube walls into contact (beyond point c on the curves). The pressures were normalized by the same values of  $P_k$  as those used by Bertram.<sup>1</sup> The computed pressure–area data for the two tubes are compared with the experimental data in Figs. 17 and 18. The corresponding tube configurations at points a, b and c are

<sup>1</sup>The comparison of the two experimental tubes in terms of normalised pressure was omitted by Bertram (1987) at the behest of a referee, but was published by Bertram (1995). As described by Bertram and Elliott (2003), slightly revised values of  $P_k$  (11.3 and 26.8 kPa) are now preferred, and are used here.

also shown on the right of the figures. There is reasonable agreement between the computed pressure–area curves and the experimental curves. In both cases, we were able to perform our computation only until point *c*, after which, numerical results were very difficult to obtain using the current approach. For the ‘thinner-walled’ tube, the point *c* represents an almost contacted configuration. However, for the thick-walled tube, the two opposite walls were still a significant distance away from contact. This is in part because we used pressure as the control parameter. The slope of the predicted pressure–area relation in Fig. 18 is small by point *c*, so  $\bar{p}$  is very ineffective as a determinant of the operating point. In both cases, once the tube buckles and the tube becomes highly compliant and sensitive to the pressure change, the numerical simulation predicts more negative transmural pressure than was observed in the experiments. This discrepancy, which increases as the tube becomes more collapsed, will be discussed further in Section 4.

#### 4. Discussion

The numerical results for the buckling tube cross-section, computed as the first test of the numerical model, were in good agreement with both the analytically predicted buckling load and the tube shapes predicted numerically by Flaherty et al. (1972).

We then proceeded to model the realistic three-dimensional collapsible tube with ends clamped to rigid tubes. The results for thinner-walled tubes were compared with Hazel and Heil’s published results (2003), and excellent agreement was found. Hazel and Heil (2003) adopted a displacement-control technique in obtaining the buckling solutions of the collapsible tube, whereby the degree of collapse was specified by prescribing the radial displacement of a control point on the tube wall. As displacement control is not an option in FIDAP, pressure control was used here instead. This caused us considerable numerical difficulties, because achieving convergence to a buckled state is extremely hard with pressure as a control parameter, as the sudden tube buckling is highly sensitive to small pressure fluctuations. To overcome this, the computation had to be carefully monitored through many intermediate stages. At each stage, an intermediate solution at lower *Re* and  $p_{\text{ext}}$  was sought, then the load parameters and *Re* were increased, and the simulation was restarted from the previous solution. Such a process was repeated until we smoothly approached the final  $p_{\text{ext}}$  and *Re*. It was especially tricky to achieve converged solutions when the load increments were large, or the Reynolds number was higher. In the end, using the pressure-control technique, we have successfully obtained results for both Stokes flow and finite-*Re* flows which agree almost identically with results by Hazel and Heil (2003).

The influence of wall thickness on the overall behaviour of the system was then studied. Two comparative situations were analysed. One compared the different tubes at the same degree of collapse (by imposing different external pressure); the other compared them when the same external pressure was applied. Finally, we also found the evolution of the twin jets emanating from the collapsed tube into a rounded H-shaped jet, as computed by Hazel and Heil (2003) for *Re* = 350, using both the thinner and thick-walled tubes. Interesting qualitative differences in secondary flow development between these two tubes were observed. The jet evolution did not reach the stage of becoming a single annulus, as observed by Bertram and Godbole (1997) for *Re* = 705 in a rigid tube deformed to include a zone of collapse.

Not surprisingly, the wall thickness affects the wall deformation significantly, as well as the fluid flow within. However, the aim of the present study is not to establish the well-known fact that a different wall thickness changes the system behaviour, but to develop a new model which is suitable for thick-walled tubes. This is important, since it is thick-walled tubes that have been extensively used in experiments, especially those by Bertram and his colleagues (Bertram, 1987; Bertram et al., 1991; Bertram and Castles, 1999).

Finally, the numerical predictions for two thick-walled tubes clamped on rigid tubes were compared with the experimental data measured by Bertram (1987). The application of the pre-stretch condition needed to emulate the experimental state introduced extra convergence problems, since the computations became even more sensitive to small pressure changes during the pressure-control manoeuvre. As a result, the pressure increments during the intermediate stages had to be much smaller than those used without the pre-stretch. The computed pressure–area curves for the thick-walled tubes are lower than the experimentally measured ones, i.e. the computed tube resists collapse more, and in Fig. 17 the computed compliance (inversely given by the slope of the pressure–area relation) is less during the collapse phase between buckling and osculation. Several concurrent reasons may explain these discrepancies. Firstly, there exists a geometrical difference between the physical problem and the computational approximation. In the experiment, the collapsible tubes were clamped at both ends over rigid tubes of slightly bigger radius than the nominal collapsible-tube radius. This was neglected in the computational domain, but is not thought to be of great import. Secondly, the experiments were performed on silicone-rubber tubing which was found to exhibit subtle signs of aging, whereas we

assumed perfectly elastic behaviour equivalent to subjecting brand-new tubing to compression. The aging in the experiments would have tended to make the real tube easier to collapse. Finally, Bertram (1987) noted that the preferred shape of unstressed tube samples was slightly oval; this again is ignored in the computed model, where the starting cross-sectional area is circular. Thus our model will be stiffer than the real tube; we think that this is the dominant experimental factor explaining the discrepancy in the level of transmural pressure at which the tube moves from buckling to osculation. Ribreau et al. (1994) have shown that oval tubes are distinctly less stiff in collapse than truly circular ones. Both of the computed tubes buckled at close to the theoretical  $\bar{p}$  value for a thinner-walled tube of  $-3$ , despite their very considerable thickness ( $-3.10$  for  $h/R_i = 0.38$ ,  $-3.22$  for  $h/R_i = 0.50$ ). The reason why the computed compliance below buckling in Fig. 17 is substantially lower than that observed is unclear; however, in this context we note that Bertram and Raymond (1991) found the incremental compliance on this limb of the pressure–area relation to be much less than the compliance measured from the overall slope. What is of considerable interest, however, is the finding that the computed thick-walled tube ( $h/R_i = 0.50$ ) was more compliant than the computed thinner one ( $h/R_i = 0.38$ ) after buckling. This accords with the relative behaviour of the two measured tubes, where the slope  $dp_{im}/dA$  during the transit from buckling to opposite-wall contact was less in the thick than the thinner tube, whether  $p_{im}$  was normalized or not. The importance of this lies in the fact that the pressure wavespeed  $c$  calculated from the Young equation ( $c = (A/\rho)(dP/dA)^{1/2}$ ) depends on  $A(dp_{im}/dA)$ ; it thus seems that the thick tube has a lower wavespeed at corresponding areas between buckling and osculation than the thinner one. This was shown in Fig. 9 of Bertram (1987), and noted in the text, but the unexpected result was not discussed further. Now, however, the numerical results provide confirmation of this finding, which runs contrary to the increase of wavespeed with wall thickness in distended tubes.

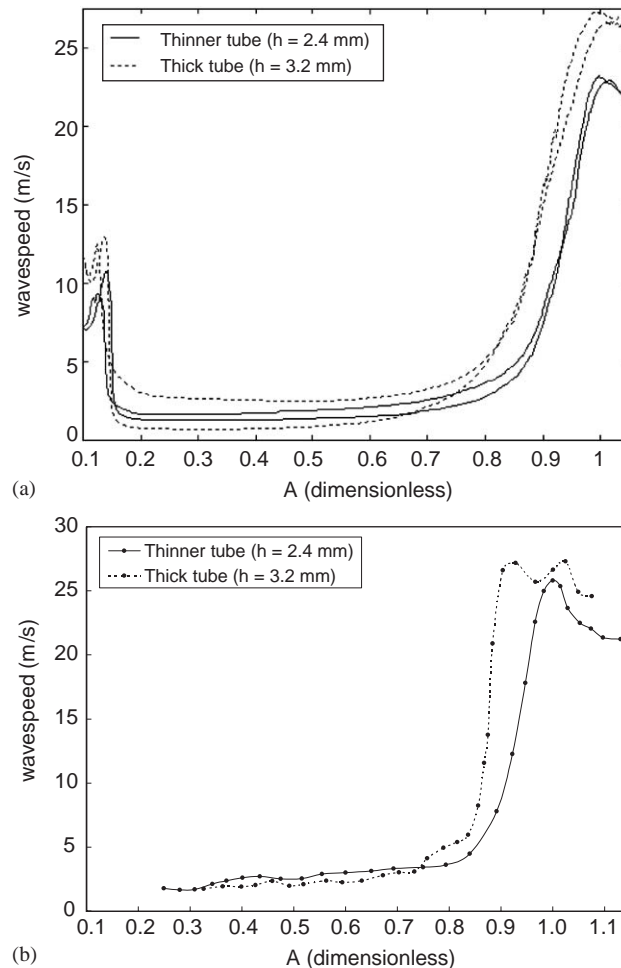


Fig. 19. (a) Wavespeed calculated by the Young equation from the pressure–area relations of the two thick-walled tubes measured by Bertram (1987); (b) same as (a), but using numerical results.

The variation of wavespeed with area for the two observed tubes is shown in Fig. 19(a). Only during collapse was this found; during recovery, the thick tube, but not the thinner one, displayed much less compliance. Experimentally, the minimum wavespeed reached (just before osculation) was about 0.66 m/s in the thick tube and 1.28 m/s in the thinner one. The corresponding numerical findings are shown in Fig. 19(b). The minimum calculated numerical values were 1.75 and 1.64 m/s, respectively, but these are minima dictated by how far along the collapse curve for each tube it was possible to go numerically, rather than by the relative compliance. Fig. 19(b) shows that over most of the low-wavespeed range, the numerical wavespeed was lower at corresponding area for the thicker tube than for the thinner one. (The difference is not as great as might be expected from inspection of the pressure–area curves in Figs. 17 and 18, where normalization of the transmural pressure by  $P_k$  compresses the thick-walled relation vertically rather more.)

It is thought that the inverse dependence of wavespeed on wall thickness may relate to proximity in parameter space to the start of a cusp catastrophe [see Bertram et al. (1991)]—what Heil and Pedley (1996) term a snap-through in the specific context of buckling. Given the known connection between minimum wavespeed and choking flow-rate in 1-D theory, and the experimentally observed association between choking conditions and oscillation (Brower and Scholten, 1975), this finding may have significance in explaining the relative prevalence of oscillation in tubes of varying wall thickness. [Theory does not necessarily support a connection between choking and oscillation for the relatively short tube of a Starling resistor, since in the latter the instability of the system is believed to be the main cause of oscillations—Luo and Pedley (1996).] All in all, remarkable qualitative and reasonably good quantitative agreement is obtained between the present simulations and Bertram's published findings on the no-flow properties of thick-walled collapsible tubes.

## 5. Conclusions

In this study, we have simulated 3-D flow in collapsible tubes using a finite-element approach and the pressure-control technique. The numerical approach was systematically and carefully validated. The effects of wall thickness beyond the thin-shell limitation were studied, and quantitative comparison was made with the thinner-walled model of Flaherty (1972) and thick-walled tube experiments by Bertram (1987), for no flow. We have confirmed the previous findings by Hazel and Heil (2003) for thinner-walled tubing, and showed the existence of significant differences if a thick-walled tube is used. Keeping the same maximal extent of collapse (by imposing a much higher external pressure), as a result of the different pattern of deformation, there are differences in the flow pattern, including disappearance of the 'four-eddy' secondary flow. We have also confirmed the counter-intuitive compliance behaviour of buckled thick-walled tubes that was observed by Bertram (1987). Most importantly, this work has set up the foundation for further quantitative comparison with Bertram's unsteady flow experiments. Finally, we have showed that by using FIDAP, it is possible to perform the complicated tasks of fluid–structure interactions. This will enable other researchers in the field to use FIDAP as an effective tool to explore new phenomena of fluid–structure interactions. Further studies on unsteady flow simulation are now under way which may lead to new insights into the physical mechanisms of the rich variety of observed self-excited oscillations.

## Acknowledgements

We wish to give special thanks to Nilesh Gandhi, support engineer of Fluent India Pvt. Ltd., and the University of Sheffield for providing a Ph.D. studentship for A.M. We also wish to thank D.A.M.T.P. of the University of Cambridge for the award of the David Crighton Fellowship to A.M., and Professor T.J. Pedley, FRS, for many useful conversations. The experiments of Bertram (1987) were funded in part by a grant from the predecessor body to the Australian Research Council.

## Appendix A

To assess the suitability of the meshes used in this work we repeated some selected analyses using different grids. In addition, we validated our results for flow in thinner-walled tube against those by Hazel and Heil (2003), obtaining excellent agreement for the two flow conditions examined. A mesh independence study for the problem described in Section 3.4 was also carried out. For the thinner-walled tube, the computational domain was discretized by using 2000 finite elements and 20 000 nodal points. An even finer mesh was then considered, which discretised the same

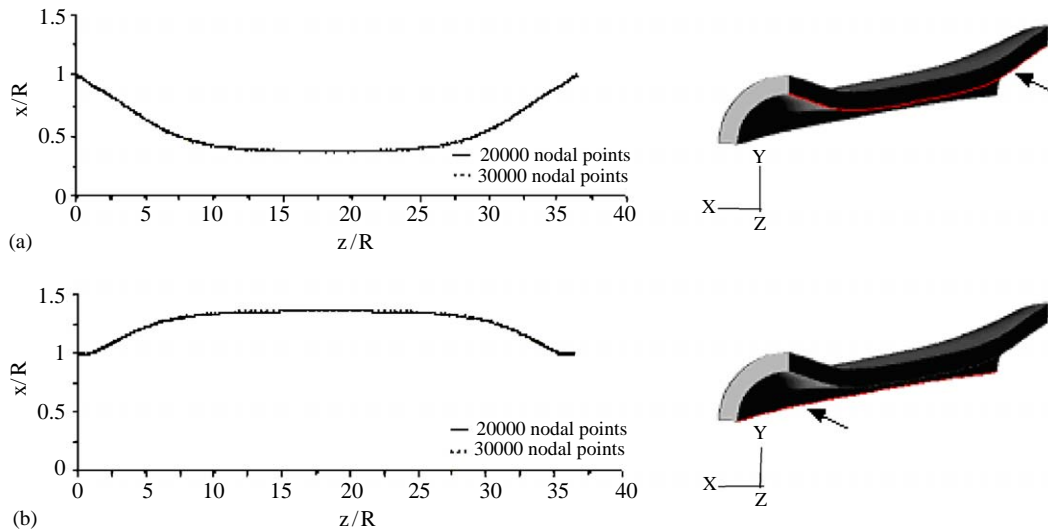


Fig. 20. Mesh-independence study based on the displacement of two edges of the computational domain.

computational domain with 3000 finite elements and 30 000 nodal points. The same value of pressure,  $\bar{p} = 4.08$ , was applied on the external surface of the elastic tube using the two different grids. The results were compared on the basis of the displacement of two different edges along the tube walls, as indicated by the arrows on the right-hand side of Fig. 20.

Fig. 20 shows that the two different grids predict almost identical collapsed deformation along the tube. The maximum relative error in calculating the displacement between the two analyses is less than 0.5%.

## References

- Bar-Yoseph, P.Z., Mereu, S., Chippada, S., Kalro, V.J., 2001. Automatic monitoring of element shape quality in 2-D and 3-D computational mesh dynamics. *Computational Mechanics* 27, 378–395.
- Berke, G.S., Green, D.C., Smith, M.E., Arnstein, D.P., Honrubia, V., Natividad, M., Conrad, W.A., 1991. Experimental evidence in the in vivo canine for the collapsible tube model of phonation. *Journal of the Acoustical Society of America* 89, 1358–1363.
- Bertram, C.D., 1987. The effects of wall thickness, axial strain and end proximity on the pressure-area relation of collapsible tubes. *Journal of Biomechanics* 20, 863–876.
- Bertram, C.D., 1995. The dynamics of collapsible tubes. In: Ellington, C.P., Pedley, T.J. (Eds.), *Biological Fluid Dynamics*. Company of Biologists Ltd., Cambridge, UK, pp. 253–264.
- Bertram, C.D., 2003. Experimental studies of collapsible tubes. In: Carpenter, P.W., Pedley, T.J. (Eds.), *Flow past Highly Compliant Boundaries and in Collapsible Tubes*. Kluwer Academic Publishers, Dordrecht, The Netherlands, pp. 51–65.
- Bertram, C.D., Castles, R.J., 1999. Flow limitation in uniform thick-walled collapsible tubes. *Journal of Fluids and Structures* 13, 399–418.
- Bertram, C.D., Elliott, N.S.J., 2003. Flow-rate limitation in a uniform thin-walled collapsible tube, with comparison to a uniform thick-walled tube and a tube of tapering thickness. *Journal of Fluids and Structures* 17 (4), 541–559.
- Bertram, C.D., Godbole, S.A., 1997. LDA measurements of velocities in a simulated collapsed tube. *ASME Journal of Biomechanical Engineering* 119, 357–363.
- Bertram, C.D., Raymond, C.J., 1991. Measurements of wave speed and compliance in a collapsible tube during self-excited oscillations: a test of the choking hypothesis. *Medical and Biological Engineering and Computing* 29, 493–500.
- Bertram, C.D., Raymond, C.J., Pedley, T.J., 1991. Application of dynamical system concepts to the analysis of self-excited oscillations of a collapsible tube conveying a flow. *Journal of Fluids and Structures* 5, 391–426.
- Binns, R.L., Ku, D.N., 1989. Effect of stenosis on wall motion—a possible mechanism of stroke and transient ischemic attack. *Arteriosclerosis* 9, 842–847.
- Brook, B.S., Pedley, T.J., 2002. A model for time-dependent flow in (giraffe jugular) veins: uniform tube properties. *Journal of Biomechanics* 35, 95–107.
- Brower, R.W., Scholten, C., 1975. Experimental evidence on the mechanism for the instability of flow in collapsible vessels. *Medical and Biological Engineering* 13, 839–845.

- Cai, Z.X., Luo, X.Y., 2003. A fluid-beam model for flow in collapsible channel. *Journal of Fluids and Structures* 17 (1), 123–144.
- FIDAP, 2002. FIDAP 8.7.0 Theory and User's Manual, Fluent, Inc.
- Flaherty, J.E., Keller, J.B., Rubinow, S.I., 1972. Post buckling behavior of elastic tubes and rings with opposite sides in contact. *SIAM Journal of Applied Mathematics* 23, 446–455.
- Griffiths, D.J., 1971. Hydrodynamics of male micturition—I: theory of steady flow through elastic-walled tubes. *Medical and Biological Engineering* 9, 581–588.
- Guyton, A.C., Adkins, L.H., 1954. Quantitative aspects of the collapse factor in relation to venous return. *American Journal of Physiology* 177, 523–527.
- Hazel, A.L., Heil, M., 2003. Steady finite-Reynolds-number flows in three-dimensional collapsible tubes. *Journal of Fluid Mechanics* 486, 79–103.
- Heil, M., Jensen, O.E., 2003. Flows in deformable tubes and channels: theoretical models and biological applications. In: Carpenter, P.W., Pedley, T.J. (Eds.), *Flow past Highly Compliant Boundaries and in Collapsible Tubes*. Kluwer Academic Publishers, Dordrecht, The Netherlands, pp. 15–50.
- Heil, M., Pedley, T.J., 1996. Large post-buckling deformations of cylindrical shells conveying viscous flow. *Journal of Fluids and Structures* 10, 565–599.
- Jensen, O.E., Heil, M., 2003. High-frequency self-excited oscillations in a collapsible-channel flow. *Journal of Fluid Mechanics* 481, 235–268.
- Kamm, R.D., Pedley, T.J., 1989. Flow in collapsible tubes: a brief review. *ASME Journal of Biomechanical Engineering* 111, 177–179.
- Ku, D.N., 1997. Blood flow in arteries. *Annual Review of Fluid Mechanics* 29, 399–434.
- Luo, X.Y., Pedley, T.J., 1995. Numerical simulation of steady flow in a 2-D collapsible channel. *Journal of Fluids and Structures* 9, 149–197.
- Luo, X.Y., Pedley, T.J., 1996. A numerical simulation of unsteady flow in a two-dimensional collapsible channel. *Journal of Fluid Mechanics* 314, 191–225.
- Luo, X.Y., Pedley, T.J., 1998. The effects of wall inertia on flow in a two-dimensional collapsible channel. *Journal of Fluid Mechanics* 363, 253–280.
- Luo, X.Y., Pedley, T.J., 2000. Multiple solutions and flow limitation in collapsible channel flows. *Journal of Fluid Mechanics* 420, 301–324.
- Pedley, T.J., 1992. Longitudinal tension variation in collapsible channels: a new mechanism for the breakdown of steady flow. *ASME Journal of Biomechanical Engineering* 114, 60–67.
- Ribreau, C., Naili, S., Langlet, A., 1994. Head losses in smooth pipes obtained from collapsed tubes. *Journal of Fluids and Structures* 8, 183–200.
- Rodbard, S., 1966. A hydrodynamics mechanism for autoregulation of flow. *Cardiologia* 48, 532–535.